VIII International Conference on Particle-Based Methods
PARTICLES 2023
U. Perego, M. Cremonesi, A. Franci (Eds)

PARTICLE-BASED SIMULATION OF CRACK PROPAGATION IN STRUCTURAL CONNECTIONS PRODUCED WITH DIRECT ENERGY DEPOSITION 3D PRINTING

J. OLSSON[1], M. ANDER[2], S. LARSSON[3], O. BORGSTRÖM[4], E. TIBUZZI[5], P. BARDEN[6] AND C.J.K. WILLIAMS[2]

[1] Chalmers Industriteknik, Sven Hultins gata 1, 412 58 Göteborg

[2] Chalmers University of Technology, Dept. of Architecture and Civil Engineering, Sven Hultins gata 6, 412 96 Gothenburg. Email: mats.ander@chalmers.se

[3] Tyréns, Lilla Badhusgatan 2, 411 21 Gothenburg

[4] Foster+Partners, ARD, Riverside, 22 Hester Rd, London SW11 4AN, UK

[5] AKT II, White collar factory, 1 Old Street Yard, London EC1Y 8AF, UK

[6] Ai Build, Unit D1 Leyton Industrial Village, Argall Avenue, London, E10 7QP, UK

Abstract: This paper explores how Force Flux Peridynamics (FFPD) can support the design of lightweight metal components in building structures produced with Direct Energy Deposition (DED) Additive Manufacturing (AM). DED is a relatively new technology that deposit metal layer-by-layer to create three-dimensional structures without the need for support structures. This process has the potential to significantly reduce the embodied carbon in building structures by reducing the weight of the structural connections and hence the weight of all other structural components [4]. However, the process applied in AM for metals can make the printed objects susceptible to defects which may compromise their structural integrity and may even lead to fracture [5]. In this paper we describe a design process for the creation of lightweight structural components while including modelling of anisotropy, yielding and brittle fracture. The central core of the process is the application of a particle method called Force Flux Peridynamics (FFPD) which is used to predict yielding and fracture. The paper thus builds upon strategies developed and defined in other publications including; the derivation of the FFPD particle method [2], a strategy for calibration of materials in paper [1], a motivation to apply this concept in the context of nodal connections for spatial structures as described in paper [3]. The specific nodal connection that is analysed in this paper is designed for rotational DED printing which creates a component with radial anisotropic mechanical properties. The node is analysed using an axial tensile and an axial compression load case where the load is applied by imposing incremental translations to the attachments where the structural members would be connected. The susceptibility to fracture in relation to the anisotropy of the printed metal is discussed.

Keywords. Force flux, Peridyanmics, SPH, 3D-printing, structural nodal connections

1 Introduction

The embodied carbon in building structures has become a critical focus in the construction industry due to its significant contribution to global carbon emissions. Building materials, such as concrete, steel, aluminium, and glass, are known to have high embodied carbon due to the energy-intensive processes involved in their production. As a result, finding alternative low-carbon materials and low-carbon production processes has become a key area of research and development.

A variety of strategies are being employed to mitigate the embodied carbon in building structures. Approaches includes, reuse and recycling of materials as well as use of renewable energy sources in manufacturing. Another strategy is the adoption of lightweight design principles to reduce material usage.

Many of the materials in the built environment such as steel, timber, concrete and brick are characterised by their mechanical complexity. Therefore, with increased material reduction concerns for safety and long-lasting resilience may arise. This has motivated the development of a particle-based simulation technique called Force Flux Peridynamics that can be used to simulate progressive fracture and thus the failure of materials. The complete derivation of FFPD can be found in [2] and the tuning of key parameters for the modelling of concrete and steel reinforcement can be found in [1]. In this paper, FFPD is applied to the modelling of the steel material produced with DED 3d printing including its anisotropic properties. The paper is focused on the application of FFPD in a design context for architecural applications with design, use and prototyping.

2 Force Flux Peridyanmics

Smoothed Particle Hydrodynamics (SPH) was first proposed in 1977 by Gingold and Monaghan [6], and is usually referred to as the first meshless method. Its inherent grid-free nature makes SPH particularly suitable for modelling large deformations and fracture, such as those encountered in rock mechanics, geoengineering, and solid-related manufacturing processes like metal extrusion and forging.

Peridynamics is another meshless method specifically aimed at the simulation of fracture in solid mechanics [7]. The continuum domain is discretised by a set of particles which are connected to their neighbours through a set of arms spanning a distance which is called the horizon. Since the arms reach further than their immediate neighbours, it is just like SPH referred to as a non-local method, and is, therefore, an appropriate approach for modelling stress concentrations and progressive fracture.

2.1 Fundamentals

Force flux Peridynamics (FFPD) presents a fusion of SPH and Peridynamics with the aim to simplify the use of varying particle sizes for solid mechanics analysis. The most central concept in FFPD is the force flux density, S, which is defined as a function of the state of stress and the fibre orientation relative to that state of stress. In 3D it is given

by

$$S = \frac{2\pi}{3} TL \tag{1}$$

where T is the tension in each fibre in a specific direction, while L represents the total length of the fibres per unit volume. The unit of L is length per unit volume, which can also be expressed as the reciprocal of length squared. Consequently, S, which is derived from T and L, has the dimensions of stress. The tension (T) of an individual fibre, as depicted in the middle image of Figure 1, is calculated from

$$T = \frac{3S}{2\pi L}, \tag{2}$$

according to Eq. (14) in [2] for the 3D case. In order to establish the discrete setup shown in Figure 1 a), it is necessary to formulate the state of stress as a function of the direction vector $\mathbf{q}$. We also want to separate the deviatoric and volumetric parts of the stress, $\boldsymbol{\tau}$ and $\bar{\sigma}$ respectively. Following the derivation in [2] section 3, Eq. (2) takes the form

$$T = \frac{3}{2\pi L} \left(\frac{5}{2} \mathbf{q} \cdot \boldsymbol{\tau} \cdot \mathbf{q} + \bar{\sigma} \right). \tag{3}$$

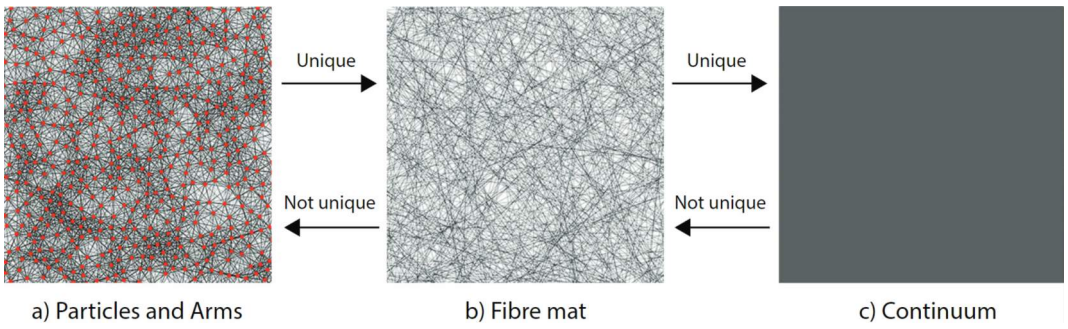

Figure 1: Discrete particles and arms on the left, fibre mat in the centre and continuum to the right.

To finally introduce the discrete particles and arms into this fibre mat-model we introduce the SPH kernel function W and the weighting of particle size in terms of mass m and density ρ. The formula for the tension in a discrete arm between particles a and b is then given by

$$T_{ab} = -\frac{m_a m_b}{\rho^2} \left(\frac{\partial W_{ab}}{\partial r_{ab}} + \frac{\partial W_{ba}}{\partial r_{ab}} \right) \left(\frac{5}{2} \mathbf{q}_{ab} \cdot \boldsymbol{\tau} \cdot \mathbf{q}_{ab} + \bar{\sigma} \right), \tag{4}$$

where $\dfrac{\partial W_{ab}}{\partial r_{ab}}$ is the derivative of the kernel function with respect the unit vector, r_{ab}, along the bond. The particle masses and kernel functions in Eq. (4) are now defined separately for particles a and b, enabling variable parameters and thus variable particle distribution

in the domain approximation. The kernel W that was used for the numerical examples in this paper is defined in section 10.1 in [2] width $k = 2$ and $\alpha = 4.5$.

The constitutive relation based on shear modulus G and bulk modulus K is introduced in the force flux expression in Eq. (110) in [2]. For the 3D case when $N = 3$ the expression for S at particle a can be written as

$$S_a\left(\mathbf{q}_{ab}\right) = 5G(\epsilon_{ab} - \epsilon_{ab}^{\text{plastic}}) + (3K - 5G)\,\bar{\epsilon}_a, \tag{5}$$

where ϵ_{ab} is the total engineering strain calculated using Pythagoras' theorem, $\epsilon_{ab}^{\text{plastic}}$ is the plastic strain and $\bar{\epsilon}_a$ is the mean strain. By inserting Eq. (5) in Eq. (3) the final expression for the arm force is given as

$$T_{ab} = -\frac{m_a m_b}{\rho^2}\left(\frac{\partial W_{ab}}{\partial r_{ab}} + \frac{\partial W_{ba}}{\partial r_{ab}}\right)\left(5G(\epsilon_{ab} - \epsilon_{ab}^{\text{plastic}}) + (3K - 5G)\,\bar{\epsilon}_a\right). \tag{6}$$

In order to finalise the ideal plastic fracture model, the inclusion of a failure condition is the remaining crucial step. In the original peridynamics formulation, arm failure was determined based on a strain limit. However, this approach is not applicable in FFPD due to the introduction of variable arm lengths.

Griffith's theory of fracture postulates that the failure stress σ_{failure} is related to the crack width c, the Young's modulus E and the surface energy γ according to

$$\sigma_{\text{failure}} \approx \sqrt{\frac{2E\gamma}{c\pi}}. \tag{7}$$

Next, we express the surface energy as $\gamma = \delta\sigma_{\text{yield tension}}$, where δ represents a constant length that correlates arm elongation with the surface energy released in the creation of new free surface during fracture. This length scale remains unaffected by the initial length of the arms. Consequently, shorter arms will necessitate a higher strain to reach fracture compared to longer arms.

The complete derivation of the theory can be found in [2].

2.2 Anisotropy

Due to the nature of the printing process the resulting specimen will be anisotropic, where material might behave differently depending on if the material is tested parallel the deposited layer or across the seam. In order to account for the anisotropy caused by the printing process in the numerical experiments presented in 5 both the yield strain limit and the elongation limit are scaled based on the direction of the arm relative to the build direction as illustrated in figure 4.

The scale factor for the yield limit is based on the relative yield strength γ_{xy} and γ_{xz} such that $s_\gamma = \gamma_{xy}\gamma_{xz}$. The scale factor for the elongation limit is based on the relative elongation between the two directions such that, $s_\delta = \delta_{xy}/\delta_{xz}$.

Under the assumption of cylindrical anisotropy produces with rotational printing the

elongation limit and yield strain for a given arm ab are then given by

$$\delta_{ab} = \delta\left(1 + s_\delta sin(\theta)\right), \tag{8}$$

$$\gamma_{ab} = \gamma\left(1 + s_\gamma sin(\theta)\right), \tag{9}$$

where θ is the angle between the arm ab and the radial vector perpendicular to the printing path. For the case when the arm is aligned with the radial direction $\theta = 0$ we have $sin(\theta) = 1$ and $\delta_{ab} = \delta + \delta s_\delta$ and $\gamma_{ab} = \gamma + \gamma s_{gamma}$. When the arm is aligned with the tangential direction when $\theta = \frac{\pi}{2}$, $sin(\theta) = 0$ and therefore $\delta_{ab} = \delta$ and $\gamma_{ab} = \gamma$.

3 Model Setup

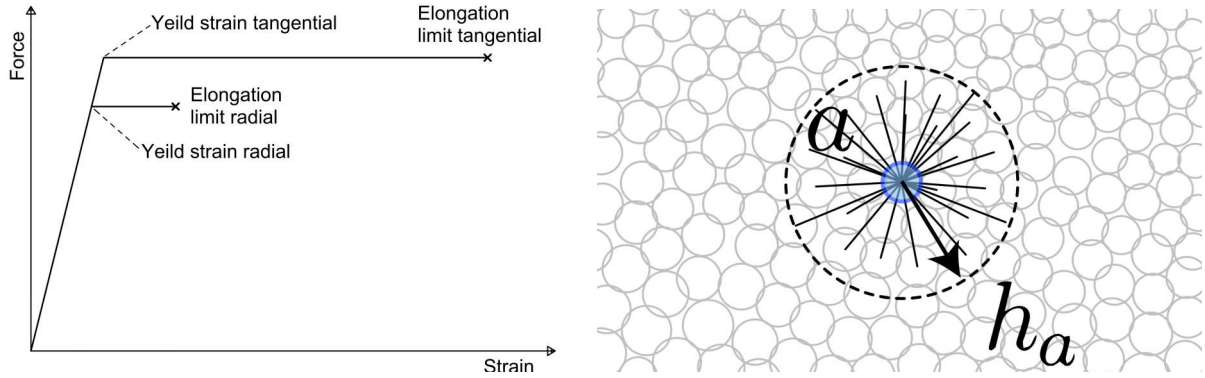

(a) Ideal plastic model

(b) Particle and arms

Figure 2: Left: Force strain diagram of the idealised plastic model used for the arms. Note that the elongation limit is 4.7 times larger and while the yield strain is 1.2 larger in the tangential direction compared to the radial direction. Right: Rectangular sub region of a continuum with a varying sized particles. All the arms are drawn for particle **a** within the horizon.

The creation of particles follows a few simple steps. The object of interest is first discritised into tetrahedral volume elements. The whole bounding box for the entire object is filled with particles and the point inclusion calculation are used to select the relevant particles using the tetrahedral elements and barycentric coordinates. The particles are then moved randomly to introduce noise in the previously regular arrangement using a Monte Carlo approach. The particular algorithm used is outline in paper [1].

Each particle is then connected to the other particles within a distance defined as the horizon. The horizon size is determined by the constant α multiplied with the particle size. The algorithm used for calculating the particles sizes is described in paper [1].

Particles and tetrahedral elements are organised in volumetric zones to reduce computation. Once particles and arms are defined the connectivity remains throughout the simulations. For simulation of fluids, soils or phase transition the connectivity could be updated with the extra computational cost.

4 Metal additive manufacturing

Following the ISO/ASTM Standard 52900 additive manufacturing (AM) techniques for metals can be split into two main categories, Directed Energy Deposition (DED) and Powder Bed Fusion (PBF) [9]. A further distinction can be made based on the heat source such as Laser (L), Electron Beam (EB), Plasma Arc (PA) or Gas Metal Arc (GMA) [10].

In DED printng, the metal is deposited in thin layers onto a build plate or a previously deposited layer. The material is usually in the form of a wire or powder, either of which is fed into the system and melted using one of the heat sources described above. DED allows for the creation of large-scale objects, with it being relatively easy to mount the equipment on, for example a robotic arm or CNC-router. The method is often used for repair, coating, or cladding applications. It is also known as laser cladding or laser metal deposition.

Laser wire DED is a specialised form of DED that employs a laser as the heat source and wire as the feedstock material. This process offers advantages in terms of efficiency of material utilisation and is particularly well suited for applications requiring high material purity and structural integrity.

PBF on the other hand (also known as Selective Laser Sintering or Selective Laser Melting) is an additive manufacturing process that involves selectively fusing or sintering layers of powdered material to create a 3D object. A thin layer of powder is spread across a build platform, and a laser selectively melts or sinters the powder according to the desired shape of the object. The process is repeated for each layer until the entire object is created. PBF is commonly used for producing complex metal parts with high precision and detail. However, it is worth noting that the maximum build volume for PBF is typically much smaller than DED, with most commercial systems offering build volumes up to 0.04 cubic metres.

4.1 Considerations on energy density

Energy density is a pivotal process parameter in the fabrication of structural components via laser DED. It is quantified as the energy transmitted by the heat source per unit volume and is contingent upon four principal parameters: laser power, deposition width, layer height, and print speed. The optimisation of these parameters is crucial for ensuring the mechanical properties and overall quality of the printed component.

Energy density directly influences the microstructure and, consequently, the mechanical properties of the printed component. A higher energy density generally results in finer microstructures and improved mechanical performance. An insufficient energy input will typically lead to pores and lack of fusion.

5 Implementation

A node from a fictitious grid shell structure is used as a test case for the simulation in this paper. The application is derived from the experience of working with lightweight structures in the context of buildings [3].

While a grid shell is typically designed for axial compression under self-weight, other

load cases (wind, snow etc) may impose bending in the structure and therefore the connection need to resist a combination of tensile and compressive stress. In order to simplify the implementation and the interpretation of the results an axial compression load and an axial tensile load are used for failure simulation of the connection. These results can be helpful and essential to understand the behaviour under bending.

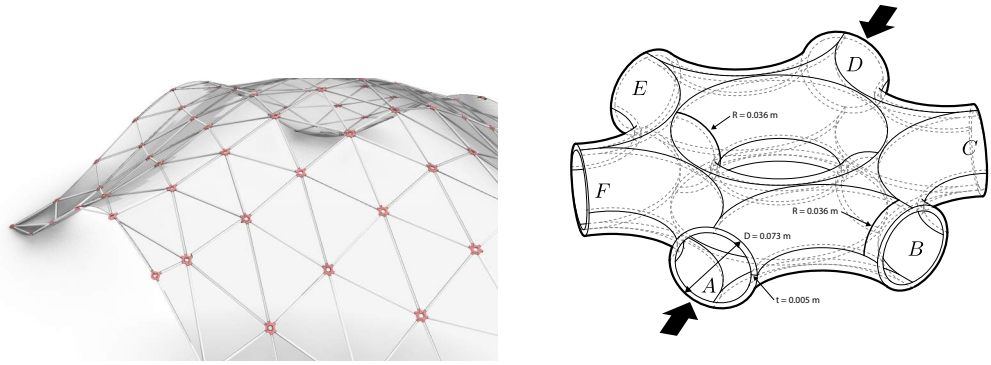

Figure 3: Left: Subsection of a fictious gridshell Right: Image of the node geometry

The nodal connection shown in figure 3 represents a typical symmetric node where 6 bars meet at one point. The node is designed to be produced with a rotational DED-L printing process which means that the layers will be organised in a circular pattern as illustrated in figure 4. The resulting mechanical properties determined by the printing process are such that the material can resist more force to reach the yield limit and can be subject to more elongation along the tangential direction which is the direction of the print head movement. The perpendicular direction (radial) is weaker and it is assumed that the change in yield strength and elongation is linearly dependent on the angle between the individual arm and the tangent and radial vectors.

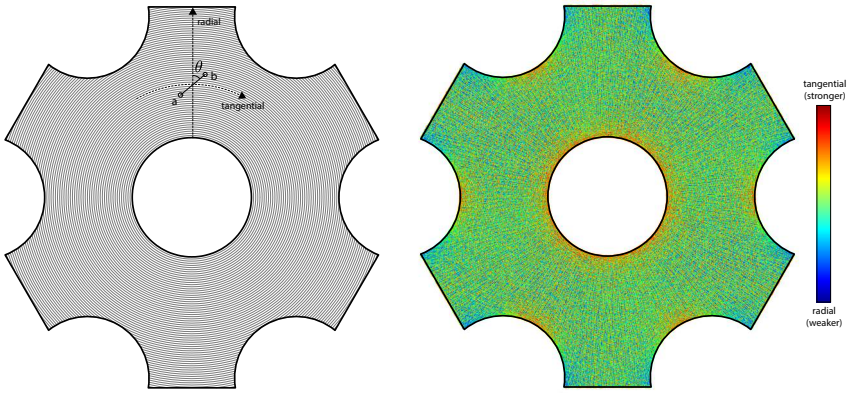

Figure 4: The build layers of the node produced with rotational printing are illustrated as lines. The illustration to the left shows the tangential direction which is the strongest (Meltio XY) and the radial direction (Meltio XZ) which is the weakest.

5.1 Physical and numerical material properties

The node is imagined to be printed using a DED-L printer such as the Meltio M450 metal printer. The physical properties of a printed test specimen produced with the M450 can be seen in table 1 which provides the input for the tuning of the numerical model. The material properties showcase significant levels of anisotropy relative to the build direction, both in terms of strength and even more so in terms of ductility.

Table 1: Material property comparison for ER70S6-steel with different means of production.

Type	Tensile (MPa)	Yield (MPa)	Elongation (%)	Hardness (HV-30)
Wrought	400 ± 50	250	23	127
Cast	415 ± 85	205	24	127
Meltio (XY)	598 ± 5	484 ± 8	71 ± 1	175
Meltio (XZ)	525 ± 12	402 ± 37	15 ± 9	175

The M450 typically can be used with ER70S6 steel for large-scale prints. Additionally, this metal has a Young's modulus of 190 GPa, a shear modulus of 73 GPa and a Poisson's ratio of 0.29.

To complete the numerical model for the FFPD simulations the elongation limit δ and the yield strength γ need to be chosen. In order to make an informed choice tuning would need to be carried out by comparing physical testing of the material with the numerical setup which is further discussed in [1]. These values are chosen to represent the weakest direction of the material. The scale factor s_γ and s_δ are calculated as 2.2 respectively, resulting $s_\gamma = 1.2$, $s_\delta = 4.7$ for the material properties listed in 1. That means the stronger direction will have a 20% increased resistance to yielding compared to the weaker direction, and a 470 % increased capacity for elongation until failure is reached.

The elongation limit is chosen as $\delta = 0.0001m$ and the yield limit to $\gamma = 0.001$. The bounding box of the node is divided into 2904 zones (22 x 22 x 6) and the node itself is populated with 208145 particles within the 24312 tetrahedral elements that are used to approximate the continuous shape of the toroidal patches. Connecting the particles within the horizon results in the creation of 12015715 arms and additional detail for the numerical setup can be found in table 2.

5.2 Solver and Loading

The numerical experiments are conducted through simulations under quasi-static conditions, employing an explicit time integration scheme known as the central difference method. To dissipate energy and achieve convergence, the particle velocities are damped using a carryover factor of 0.98. This means that the velocities from the previous time step are multiplied by 0.98 in each cycle. The primary objective is to optimally dampen

Table 2: Numerical model described in numbers.

tetrahedron count = 24312	bounding box = $(0.31, 0.32, 0.073)$ m
object volume = 0.00078915 m^3	number of zones = 2904
number of particles = 208145	number of arms = 12015715
arms per particle $\approx$ 57	average arm length = 0.0033 m

the fundamental mode of oscillation. Empirical evidence suggests that for larger models, a value closer to 1.0 is preferable.

The loading is applied to the particles with a set distance of 0.03 m from the boundary at bar attachments A and D. These particles are attached to a bed of virtual springs which are used to transfer the load from a virtual plate which is moving with small increments of $2e-7$ m per iteration. The plate is moving away from the bar attachments at A and D in the case of a tensile load case and towards the bar attachments in the compression load case. The virtual springs have s stiffness which is k = 1.0e6, initial length $l = 1e-7$. The same approach is described in more detail in [1].

5.3 Results

The results from the tension test indicates that there is a load transfer issue at the bar attachment since the node fails in the region with that smallest cross-section area. For the compression load case on the other hand the failure is better understood as a buckling or wrinkling of the region at each of the two sides where the attachments for A and D transition into the main body of the node.

5.3.1 Tension load case

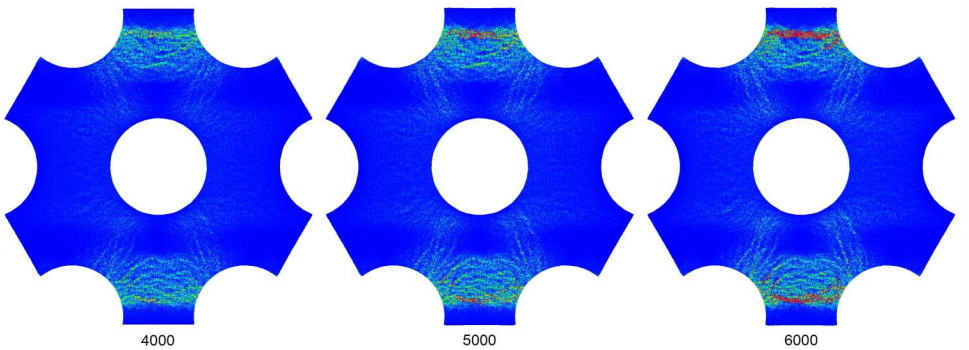

Figure 5: Top view of three stages of the progressive failure of the node when it is subject to a tensile load case. The arms are colored based on the plastic elongation limit δ such that blue arms are still in the elastic range and red arms are stretched to failure. The numbers represent the number of load steps needed to reach this state of deformation.

5.3.2 Compression load case

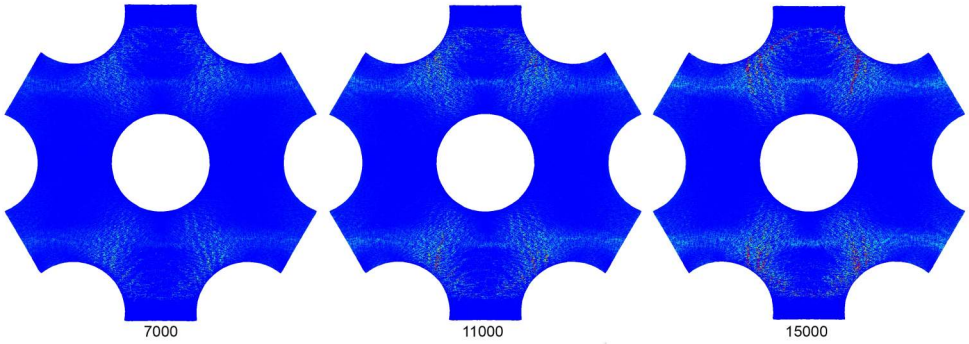

Figure 6: Top view of three stages of the progressive failure of the node when it is subject to a compressive load case. The arms are colored based on the plastic elongation limit δ such that blue arms are still in the elastic range and red arms are stretched to failure. The numbers represent the number of load steps needed to reach this state of deformation.

6 Manufacturing Process

6.1 Robotic 3D Printing in Large Format Additive Manufacturing

Robotic 3D printing serves as a specialised subset of Large Format Additive Manufacturing (LFAM), integrating a material deposition system with a multi-axis robotic arm. Unlike gantry systems, robotic arms allow full control over the angle of deposition due to the yaw, pitch and roll axes, permitting more dynamic printing angles and techniques. This combination results in a versatile apparatus capable of fabricating large geometries and avoiding the need for support structures—a limitation often encountered with conventional 3-axis gantry systems.

6.2 Apparatus and Toolpath Generation

The nodal component under investigation was fabricated by Ai Build, utilising their proprietary industrial slicing software, AiSync. The printing process employed a Meltio Engine in conjunction with a KUKA 6-axis robotic arm and a 2-axis rotary table, thereby enabling 8 degrees of freedom.

Ai Build employed a radial slicing methodology which leveraged the rotary table to eliminate overhangs that conventionally restrict printability in horizontal slicing paradigms. Throughout the manufacturing process the print head remained vertically oriented, while the component itself was subjected to rotation by the two-axis rotary table, enabling the variation of printing angle required to print the part without overhang support.

6.3 Node Fabrication

In employing the radial slicing approach, a supporting pipe, formed from the same material, was affixed to the external axis and served as the foundational substrate for

subsequent layer deposition. The deposition was initiated close to the central axis and the part progressively built outward. The pipe was integrated into the final component and severed at both ends upon completion. This methodology could present a viable avenue for future mass production, enabling the simultaneous printing of multiple nodes along a singular pipe.

The node was fabricated using a 1mm diameter 316L stainless steel wire, adhering to Meltio's recommended process parameters to ensure a fully dense structure with optimal fusion and a reported densification of greater than 99.99% [8]

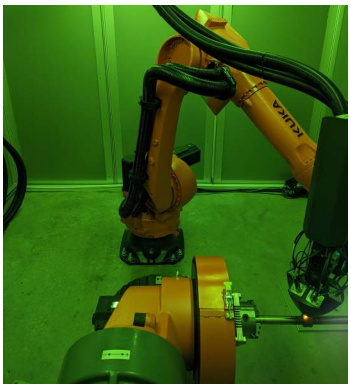

Figure 7: Left: Completed node affixed to the supporting rod and rotary table. Right: Integrated Meltio Engine, KUKA robotic arm, and rotary table during node fabrication.

7 Discussion

The fracture patterns obtained in the tensile test indicate the expected sensitivity for tension in the radial direction, given the lesser strength and ductility in this direction.

The compressive load case can sustain much larger levels of load and the fracture pattern indicate buckling and wrinkling of the relatively thin metal structure.

The results presented in this paper suffer from first and foremost two limitations. The first limitation is the choice of parameters δ and γ which is not derived from the real material testing but rather chosen based on assumptions. The real material ER70S6 is most likely more ductile so in that sense the choice of parameters are on the conservative side concerning fracture.

The second limitation is related to the discretisation of the model. Objects produced with DED-L printing obtain a rather rough surface finish with a variable thickness. However, this thickness variation does not stand in proportion to the variable thickness obtained by the irregular particle distribution. The irregularity also impose larger variation in the continuum properties than would be expected in the microscopic scale of a metal printed with DED-L, effectively adding an other conservative assumption that would weaken the object.

Future work involves calibration of the δ and γ parameters using physical testing of printed material test samples. The production of a real structural node would also enable comparison between analysis and physical testing to validate the FFPD approach.

Acknowledgements

We greatly appreciate financial support from the Chalmers Foundation, Sven Tyrén's Foundation and the Swedish research councils: Formas, Vinnova and Energimyndigheten in the project Smart Built Environment: Digitalisering och industrialisering för ett hållbart samhällsbyggande 2019.

REFERENCES

[1] J. Olsson, M. Ander, C.K.J. Willaims. *The numerical simulation of standard concrete tests and steel reinforcement using force flux peridynamics*. Structural Concrete (2022).

[2] J. Olsson, M. Ander, C.J.K. Williams. *The Use of Peridynamic Virtual Fibres to Simulate Yielding and Brittle Fracture*. Journal of Peridynamics and Nonlocal Modeling, Vol. 3. No. 4. 348-382 (2021).

[3] F. Aish and M. Ander and E. Hryha and J. Olsson and M. Tsigkari and C.J.K. Williams. *Form Finding Nodal Connections in Grid Structures*. Conference proceedings: IASS Boston (2018).

[4] Wolf, Catherine De. *Low Carbon Pathways for Structural Design: Embodied Life Cycle Impacts of Building Structures*. MIT, Boston, Phd Thesis, (2017).

[5] Dirisu, Philip and Ganguly, Supriyo and Mehmanparast, Ali and Martina, Filomeno and Williams, Stewart. *Analysis of fracture toughness properties of wire + arc additive manufactured high strength low alloy structural steel components*. Materials Science and Engineering: A, Vol.765, (2019).

[6] R.A. Gingold and J.J. Monaghan. *Smoothed particle hydrodynamics: theory and application to non-spherical stars* Oxford University Press. Monthly Notices of the Royal Astronomical Society. Vol 181. No 3, 375–389 (1977).

[7] S.A. Silling. *Reformulation of elasticity theory for discontinuities and long-range forces*, Journal of the Mechanics and Physics of Solids (2000), Vol 48, no 1, 175–209.

[8] Directed metal 3d SL. *Printing Parameters and their Effects on Part Density*, Meltio Printing Guide. (2023).

[9] ISO/ASTM52900. *Additive manufacturing - General-principles - Terminology*, International Standard ISO-Standard ISO. https://www.iso.org/obp/ui/#iso:std:iso-astm:52900:dis:ed-2:v1:en (2021)

[10] DebRoy, T. and Wei, H. L. and Zuback, J. S. and Mukherjee, T. and Elmer, J. W. and Milewski, J. O. and Beese, A. M. and Wilson-Heid, A. and De, A. and Zhang, W. *Additive manufacturing of metallic components – Process, structure and properties*. Progress in Materials Science. (2018). vol 92, 112-224